

Can Eccentric Binary Black Hole Signals Mimic Gravitational-Wave Microlensing?

Anuj Mishra^{1, 2, *} and Apratim Ganguly^{2, †}

¹International Centre for Theoretical Sciences, Tata Institute of Fundamental Research, Bangalore 560089, India

²The Inter-University Centre for Astronomy and Astrophysics (IUCAA), Post Bag 4, Ganeshkhind, Pune 411007, India

Gravitational lensing in the wave-optics regime imprints characteristic frequency-dependent amplitude and phase modulations on gravitational-wave (GW) signals, yet to be detected by ground-based interferometers. Similar modulations may also arise from orbital eccentricity, raising the possibility of degeneracies that could lead to false microlensing claims. We investigate the extent to which eccentric binary black hole (BBH) signals can mimic microlensing signatures produced by an isolated point-mass lens. With a simulated population of eccentric signals using numerical relativity simulations and TEOBResumS-Dalí waveform model, we perform a Bayesian model-comparison study, supported by a complementary *mismatch* analysis. We find a strong degeneracy for high eccentricities, low total masses, and high signal-to-noise ratios (SNRs): under these conditions, quasicircular microlensed model can be strongly favored over quasicircular unlensed model, even when the true signal is unlensed. For moderate SNRs (~ 30), binaries with $M_{\text{tot}} \lesssim 100 M_{\odot}$ and eccentricity $e \gtrsim 0.4$ are particularly susceptible to misclassifications. In such cases, inferred microlens parameters exhibit well-constrained posteriors despite being unphysical. Crucially, the degeneracy is completely removed when the recovery uses waveform models that incorporate eccentricity, which overwhelmingly favors the eccentric hypothesis over microlensing. Our results demonstrate that any event exhibiting strong Bayesian evidence for microlensing should also be analyzed with eccentric waveform models and vice-versa to avoid false positives and biased astrophysical inference. This work contributes to developing robust strategies for interpreting signals in the era of precision GW astronomy.

I. INTRODUCTION

The growing catalog of gravitational wave (GW) detections from compact binary coalescences (CBCs) by the LIGO [1], Virgo [2], and KAGRA [3–6] (LVK) Collaboration has opened a precision era of GW astronomy. With over 200 confident detections reported to date [7–11], and with the anticipated sensitivities of next-generation detectors such as the Einstein Telescope (ET) [12, 13], Cosmic Explorer (CE) [14–16], LISA [17], and DECIGO [18], the detection of subtle physical signatures in the waveform is becoming increasingly important. Two such signatures of particular astrophysical interest are orbital eccentricity and gravitational lensing.

Gravitational lensing is a phenomenon that arises from the interaction between mass inhomogeneities along the line of sight and the propagation of radiation [19, 20]. While gravitational lensing has been extensively observed in the electromagnetic spectrum [e.g., 21, 22], it has yet to be confidently observed in the context of GWs [23–25], though several intriguing candidates have been proposed [26–28]. The detection of lensing signatures in GWs holds immense significance: enable tests of general relativity [29, 30], probe fundamental physics [31], improve measurements of cosmological parameters [32, 33], estimates of high-redshift merger rates [34], and enhanced source localization [35].

In the geometric-optics regime, gravitational lensing by galaxy or galaxy cluster-scale lenses can produce multiple copies (or, *images*) of a GW signal, known

as *strong* lensing, with distinct arrival times, magnifications, and phases [26, 32, 36–51]. These images fall into three categories: Type I (minima), Type II (saddle-point) [26, 40, 48, 52], and Type III (maxima), whose phases differ by a Morse phase of 0, $-\pi/2$, and $-\pi$, respectively. For smaller lens masses, where the GW wavelength becomes comparable to the Schwarzschild scale, wave-optics effects become important and produce frequency-dependent modulations in the observed signal, known as *microlensing* [53–67]. Ground-based detectors are sensitive to microlensing by compact objects with masses $\sim 10\text{--}10^5 M_{\odot}$, encompassing stellar-mass compact objects and intermediate-mass black holes. Searches in this band are especially valuable for constraining the compact dark matter fraction in this mass range [68], a region that is not yet well constrained.¹

At the same time, several LVK events show hints of measurable eccentricity [69–78], even though the majority of binaries formed through isolated stellar evolution are expected to circularize by ~ 10 Hz [79–81]. While negligible eccentricities are expected for binaries formed through isolated stellar evolution [82], several alternative formation channels can yield highly eccentric systems ($e \gtrsim 0.5$ at 10 Hz) at small separations [83]. Such channels include primordial black hole binaries [84], dynamical encounters in dense stellar environments [85], and the evolution of isolated triple systems [86].

While the rate of expected microlensed signals remains uncertain, the impact of non-zero orbital eccentricity is expected to become increasingly significant as we probe earlier stages of binary evolution or as detector sensi-

* anuj.mishra@icts.res.in

† apratim@iucaa.in

¹ We note that GWs also yield indirect constraints on compact dark matter fractions through the observed merger-rate density.

tivities improve [87–89]. Consequently, eccentric GW signals are expected to be detected by future ground- and space-based observatories such as CE, ET, DECIGO, and LISA. In case of eccentric signals, the usual oscillations in the strain at twice the orbital frequency are modulated by an oscillating envelope with a frequency lower than the orbital frequency, corresponding to the pericenter precession [90]. Unlike the effects of binary masses, aligned spins, and tidal deformabilities, which are distinguishable from diffraction induced modulations because those do not cause oscillations in the amplitude and in the unwrapped phase of the frequency-domain waveform, the oscillation caused by the orbital eccentricity can potentially be mimicked by the modulations produced by wave-optics microlensing [91]. If eccentricity is not modeled during inference, these effects may be confused and potentially lead to false microlensing claims.

In this work, we focus on microlensing by an isolated point-mass lens and show that such biases can indeed arise when eccentricity is ignored in the analyses. Using Numerical Relativity and `TEOBResumS-Dali` eccentric waveforms, together with both Bayesian model-comparison studies and *mismatch* analyses, we examine whether unlensed eccentric BBH signals can be misidentified as microlensed when analyzed with quasi-circular templates, quantify the regions of parameter space where this confusion is most severe, and demonstrate that the degeneracy is fully broken when eccentric waveform models are used in recovery.

The paper is organized as follows. Section II describes the microlensing framework and the computational setup. In Sec. III and Appendix A, we present the results of our Bayesian model-comparison study and mismatch analyses. We conclude in Sec. IV with implications for future microlensing searches in the precision-GW era.

II. METHODOLOGY: COMPUTATIONAL SETUP AND BAYESIAN MODEL COMPARISON

In this section we summarize the microlensing formalism used to generate and recover microlensed waveforms, describe the injection and parameter estimation configuration employed throughout this work, and outline the Bayesian model comparison framework used to discriminate competing hypotheses.

A. Microlensing

In the wave-optics regime, microlensing modifies the frequency-domain GW strain by a complex frequency-dependent amplification factor. The lensed waveform is related to the unlensed waveform by the multiplicative kernel

$$h_{\text{ML}}(f; \boldsymbol{\lambda}, \boldsymbol{\lambda}_{\text{L}}) = F(f; \boldsymbol{\lambda}_{\text{L}}) h_{\text{UL}}(f; \boldsymbol{\lambda}), \quad (1)$$

where h_{UL} and h_{ML} denote the unlensed and microlensed BBH waveform, respectively, $\boldsymbol{\lambda}$ is the set of intrinsic and

extrinsic binary parameters, and $\boldsymbol{\lambda}_{\text{L}}$ are the microlens parameters. The complex amplification factor $F(f)$ encodes the frequency-dependent diffraction and interference effects [53–56].

For concreteness, we adopt the canonical isolated point-mass lens model [56], in which the amplification factor is fully specified by two parameters: the redshifted lens mass $M_{\text{L}}^z \equiv M_{\text{L}}(1+z_{\text{L}})$ and the dimensionless impact parameter y (in units of the Einstein radius). In closed form, $F(f)$ is given by [56]

$$\begin{aligned} F(f; M_{\text{L}}^z, y) &\equiv F(\omega, y) \\ &= \exp \left\{ \frac{\pi\omega}{4} + \frac{i\omega}{2} \left[\ln \left(\frac{\omega}{2} \right) - 2\phi_{\text{m}}(y) \right] \right\} \quad (2) \\ &\times \Gamma \left(1 - \frac{i\omega}{2} \right) {}_1F_1 \left(\frac{i\omega}{2}, 1; \frac{i\omega y^2}{2} \right), \end{aligned}$$

where $\omega = 8\pi GM_{\text{L}}^z f / c^3$ represents the dimensionless frequency that depends solely on M_{L}^z for a given dimensionful frequency f , and $\phi_{\text{m}}(y)$ is a frequency-independent quantity depending only on y , given by $\phi_{\text{m}}(y) = (x_{\text{m}} - y)^2/2 - \ln(x_{\text{m}})$, where $x_{\text{m}} = (y + \sqrt{y^2 + 4})/2$. Equations (1)-(2) are sufficient to generate microlensed strains from any frequency-domain unlensed waveform model.

All microlensed injections and parameter inference studies in this work use a custom frequency-domain implementation that augments standard BBH models with the two microlens parameters (M_{L}^z, y) . The implementation is publicly available in the `GWMAT` package.²

Unless otherwise stated, we adopt weakly informative priors commonly used in microlensing searches:

$$\begin{aligned} p(\log_{10} M_{\text{L}}^z) &\propto \text{Uniform}(-1, 5), \\ p(y) &\propto y \quad \text{for } y \in (10^{-3}, 5). \end{aligned} \quad (3)$$

The $p(y) \propto y$ prior follows from simple geometric/isotropic arguments for random source-lens alignments[92]. For cases where we observe the corresponding 1D-marginalized posteriors *railing* against the prior bounds, we broaden the priors accordingly to avoid artificial truncation.

B. Injection strategy and parameter-estimation setup

To study the biases in microlensing searches ignoring eccentricity in the recovery templates, we consider simulated BBH signals, or *injections*. These injections are done in the detector network of LIGO-Virgo with the projected Advanced LIGO and Virgo sensitivities³ [93].

² <https://git.ligo.org/anuj.mishra/gwmat/>

³ For LIGO detectors, we use the PSD given in [here](#). While for Virgo, we use the PSD available [here](#).

To isolate modeling biases and avoid noise systematics, i.e., biases due to specific noise realizations, we do not add noise to our injections. In other words, we assume a realization of Gaussian noise that takes its mean value (zero) at every time step. This avoids stochastic fluctuations due to particular noise realizations and highlights systematic waveform-modeling effects.

Throughout this work, we use the publicly available Bayesian inference library `Bilby` [94, 95] for performing parameter estimation runs and computing the evidences. Specifically, we use `Dynesty` [96] nested sampler with the ‘acceptance-walk’ method for the Markov-Chain Monte-Carlo (MCMC) evolution as implemented in `Bilby`. We evaluate the likelihood from a lower frequency of $f_{\text{low}} = 20$ Hz up to the Nyquist frequency of $f_{\text{high}} = 1024$ Hz, under the assumption of stationary and Gaussian noise which is uncorrelated across detector. Our default priors are chosen to be agnostic and sufficiently wide to cover the region of the parameter space where the posteriors have support. For quasicircular BBH waveform models, which are usually 15 dimensional, they are uniform in (redshifted) component masses, uniform in spin magnitudes, isotropic in spin orientations, isotropic in binary orientation, uniform in merger time and coalescence phase, isotropic in sky location, and our distance prior corresponds to a uniform merger rate in comoving volume and time.

C. Bayesian model comparison and interpretation

To compare between any two models/hypotheses, say, \mathcal{H}_1 and \mathcal{H}_2 , we utilize Bayesian model comparison scheme. Specifically, we make use of the Bayesian evidence (or marginal likelihood) $\mathcal{Z} = \int d\boldsymbol{\theta} \pi(\boldsymbol{\theta}) \mathcal{L}(\mathbf{d}|\boldsymbol{\theta})$, which is an n -dimensional integral. Here, $\boldsymbol{\theta} \in \mathbb{R}^n$ is the parameter space describing the signal, $\pi(\boldsymbol{\theta})$ is the prior expectation we have about $\boldsymbol{\theta}$, and $\mathcal{L}(\mathbf{d}|\boldsymbol{\theta})$ is the likelihood of observing the data \mathbf{d} given $\boldsymbol{\theta}$. Under the assumption that the two models are equally likely, we set their prior probabilities to be equal (i.e., $p(\mathcal{H}_1) = p(\mathcal{H}_2)$). The two models can then be compared using their Bayes factors as:

$$\frac{p(\mathcal{H}_2|\mathbf{d})}{p(\mathcal{H}_1|\mathbf{d})} = \frac{p(\mathbf{d}|\mathcal{H}_2)}{p(\mathbf{d}|\mathcal{H}_1)} = \frac{\mathcal{Z}_{\mathcal{H}_2}}{\mathcal{Z}_{\mathcal{H}_1}} \equiv \mathcal{B}_{\mathcal{H}_1}^{\mathcal{H}_2}, \quad (4)$$

$$\Rightarrow \log_{10} \mathcal{B}_{\mathcal{H}_1}^{\mathcal{H}_2} = \log_{10} \mathcal{Z}_{\mathcal{H}_2} - \log_{10} \mathcal{Z}_{\mathcal{H}_1}. \quad (5)$$

In practice we compare (i) the quasicircular microlensed (QCML) hypothesis $\mathcal{H}_{\text{QCML}}$ to the quasicircular unlensed (QCUL) hypothesis $\mathcal{H}_{\text{QCUL}}$, and (ii) the eccentric unlensed (EccUL) hypothesis $\mathcal{H}_{\text{EccUL}}$ to $\mathcal{H}_{\text{QCUL}}$, thereby quantifying whether eccentricity can masquerade as microlensing under standard quasicircular analyses.

Interpretation of Bayes Factors: In this work, we mainly use Jeffreys’ criterion [97] for interpreting Bayes factors. However, it only provides a conservative estimate for two main reasons:

- Since the injections are performed in zero noise, fluctuations associated with specific noise realizations are not accounted for. Such fluctuations can increase the uncertainty in the Bayes factor and may drive it to even higher values.
- Evidence integrals depend on priors; for $\mathcal{H}_{\text{QCML}}$, adding microlens parameters enlarges the prior volume and introduces an Occam penalty. Moreover, The $p(y) \propto y$ prior preferentially weights weakly microlensed (large y) regions where $F(f) \rightarrow 1$, reducing evidence for microlensing unless the data show substantial likelihood gain at small y .

Therefore, we expect the preference for the microlensing hypothesis to increase when an agnostic uniform prior on y is used, and the uncertainty to increase in the presence of noise. The Bayes factors reported here should thus be regarded as conservative estimates.

III. RESULTS

We present two complementary sets of studies designed to quantify the extent to which orbital eccentricity can mimic wave-optics gravitational lensing and to determine when that degeneracy can be broken. In Sec. III A, we analyze highly reliable NR eccentric injections, while in Sec. III B, we perform a larger controlled injection campaign using `TEOBResumS-Dali` waveforms to explore the degeneracy across total mass, mass ratio, and eccentricity. In both cases, we first analyze the injections with quasicircular templates and then with eccentric templates to demonstrate how including the correct physics removes the confusion.

A. Numerical Relativity Injections

In this section, we examine whether a standard (unlensed) eccentric BBH GW signal can be incorrectly classified as a quasicircular microlensed signal when eccentricity is ignored during the analysis. To perform this study, we use some of the most accurate eccentric GW signals currently available, obtained entirely from numerical relativity (NR) simulations. Specifically, we select three non-spinning eccentric simulations from the latest (third) SXS catalog release [99], with SXS IDs $\{\text{SXS:BBH:2524, SXS:BBH:3957, SXS:BBH:2544}\}$, corresponding to mass ratios $q = \{1, 2, 3\}$, respectively, and matching quasicircular counterparts $\{\text{SXS:BBH:1132, SXS:BBH:1222, SXS:BBH:2265}\}$. For the injections, we utilize the highest available resolution of these simulations and use extrapolated waveforms with extrapolation order $N=2$, considering only the dominant $(\ell, |m|) = (2, 2)$ mode.

For each eccentric NR case, the total redshifted binary mass is chosen such that the periastron frequency of the dominant $(\ell, |m|) = (2, 2)$ mode crosses 20 Hz at the NR

Table I: Bayesian model comparison between the QCUL and QCML hypotheses for six zero-noise non-spinning numerical-relativity injections from the SXS catalog, corresponding to QCUL and EccUL signals, each with mass ratios (q) of $\{1, 2, 3\}$. The total binary masses (M) for the eccentric injections are chosen such that all the signal content above 20 Hz is retained (see Sec. 2G of [98] for further details). We set the same M for both EccUL and the corresponding QCUL injection with the same q for comparison. For each eccentric injection, we quote the gauge-independent eccentricity measured at 20 Hz ($e_{20\text{ Hz}}^{\text{gw}}$) using the `gw_eccentricity` package. The Bayes factor comparing the QCML and QCUL hypotheses is denoted as $\log_{10} \mathcal{B}_{\text{QCUL}}^{\text{QCML}}$. Additionally, for each case, we list the inferred microlens parameters, ($\log_{10} M_L^z$) and (y), along with the Jensen–Shannon divergence (JSD) values between their 1D marginalized posteriors and corresponding priors. Finally, we also provide the Bayes factor values between the EccUL and QCUL models for reference. The extrinsic parameters of the signal are kept same as that of GW150914, except that of the luminosity distance, which is scaled to achieve a network optimal SNR of 100, and the inclination is set to 0.

SXS ID	Orbit type	q	M/M_\odot	$e_{20\text{Hz}}^{\text{gw}}$	$\log_{10} \mathcal{B}_{\text{QCUL}}^{\text{QCML}}$	$\log_{10} M_L^z$	$\text{JSD}(M_L^z)^a$	y	$\text{JSD}(y)^a$	$\log_{10} \mathcal{B}_{\text{QCUL}}^{\text{EccUL}}$
SXS:BBH:1132	quasicircular	1	75.0	-	-0.55	$-0.16^{+0.60}_{-0.57}$	0.57	$3.60^{+0.99}_{-1.46}$	0.05	-0.38
SXS:BBH:1222	quasicircular	2	77.6	-	-0.55	$-0.13^{+0.67}_{-0.59}$	0.57	$3.63^{+0.97}_{-1.43}$	0.05	-0.59
SXS:BBH:2265	quasicircular	3	87.1	-	-0.50	$-0.12^{+0.75}_{-0.60}$	0.55	$3.68^{+0.94}_{-1.46}$	0.05	-0.34
SXS:BBH:2524	Eccentric	1	75.0	0.2893	13.86	$4.88^{+0.02}_{-0.02}$	0.79	$2.64^{+0.12}_{-0.09}$	0.72	471.81
SXS:BBH:3957	Eccentric	2	77.6	0.2912	8.91	$1.89^{+0.04}_{-0.04}$	0.79	$2.58^{+0.18}_{-0.16}$	0.67	488.81
SXS:BBH:2544	Eccentric	3	87.1	0.2914	32.32	$5.00^{+0.01}_{-0.01}$	0.79	$2.14^{+0.05}_{-0.04}$	0.77	544.51

^a Jensen–Shannon divergence value between the prior and the 1D marginalized posterior density for the parameter quoted in parenthesis.

relaxation time⁴ giving $M_{\text{tot}} \approx \{75.0, 77.6, 87.1\} M_\odot$ (we follow the prescription in Sec. 2G of [98]). The corresponding gauge independent eccentricities measured at 20 Hz, computed using the `gw_eccentricity` package [98, 100], are $e_{20\text{Hz}}^{\text{gw}} \approx \{0.2893, 0.2912, 0.2914\}$.

We choose the inclination to be 0 (face-on binary) so that only the $m = 2$ [spin-(−2)-weighted] spherical harmonic modes of the signal contribute, avoiding higher-order modes that would require significantly longer NR simulations for the masses considered here. The luminosity distance is adjusted to produce a network optimal SNR of 100 for each injection. Other extrinsic parameters are set to the median posterior values inferred for GW150914⁵ [101].

For parameter estimation and evidence computation with `Bilby`, we use only the dominant $(\ell, |m|) = (2, 2)$ mode (same as in the injections). To compare $\mathcal{H}_{\text{QCML}}$ and $\mathcal{H}_{\text{QCUL}}$, we compute $\log_{10} \mathcal{B}_{\text{QCUL}}^{\text{QCML}}$, employing the `IMRPhenomXP` waveform model [102–104]. The sampler settings are `nlive=1000`, `n-accept=60`, and `n-parallel=3` per injection, with a stopping criterion of $\Delta \log \mathcal{Z} < 0.1$.

Table I summarizes the model comparison results. Notably, all eccentric NR injections show very strong support for the microlensing hypothesis ($\log_{10} \mathcal{B}_{\text{QCUL}}^{\text{QCML}} > 1$). The corresponding inferred microlens parameters (red shaded

curves; right panel in Fig. 1) also differ noticeably from their prior distributions (black dashed curves), with well-localized one-dimensional marginalized posteriors. This behavior is quantified by the Jensen–Shannon divergence (JSD) between the prior and posterior distributions. For y , JSD increases from ~ 0.05 for the QCUL injections to $\gtrsim 0.7$ for the EccUL injections. For $\log_{10} M_L^z$, it increases from ~ 0.55 (QCUL) to ~ 0.79 (EccUL). The comparatively larger JSD for $\log_{10} M_L^z$ in the QCUL injections is expected, as this parameter is typically better constrained in the weak-microlensing regime (see Appendix A of [62]). By contrast, all quasicircular injections yield $\log_{10} \mathcal{B}_{\text{QCUL}}^{\text{QCML}} < 0$, decisively rejecting the microlens hypothesis, as expected. Their inferred 1D-marginalized posteriors for y closely follow the prior (blue shaded curves; left panel in Fig. 1), and their inferred $\log_{10} M_L^z$ values remain below unity, consistent with the expectations for unlensed systems.

Lastly, we also perform an eccentric-versus-quasicircular model-comparison study by computing $\log_{10} \mathcal{B}_{\text{QCUL}}^{\text{EccUL}}$. To avoid waveform–model systematics, we use the same waveform model for both hypotheses: `TEOBResumS-Dali`⁶ [105–111], a state-of-the-art eccentric IMR waveform model that is currently publicly available. For the EccUL hypothesis, the eccentricity is treated as a free parameter with a uniform prior in $[0, 0.98]$, defined at the periastron frequency, which is set equal to the waveform starting frequency of $f_{\text{start}} = 20$ Hz; the true anomaly has a uniform prior on $[0, 2\pi]$; the in-plane spin components are fixed to zero;

⁴ The time removed from the start of the NR time series to ensure the junk radiation is negligible [99].

⁵ Posterior samples available at [Zenodo](#). We use the median of the 1D-marginalized posteriors from the ‘C01:Mixed’ channel of ‘IGWN-GWTC2p1-v2-GW150914_095045_PEDataRelease_mixed_cosmo.h5’.

⁶ Version v1.1.0, commit hash `6de7c26`.

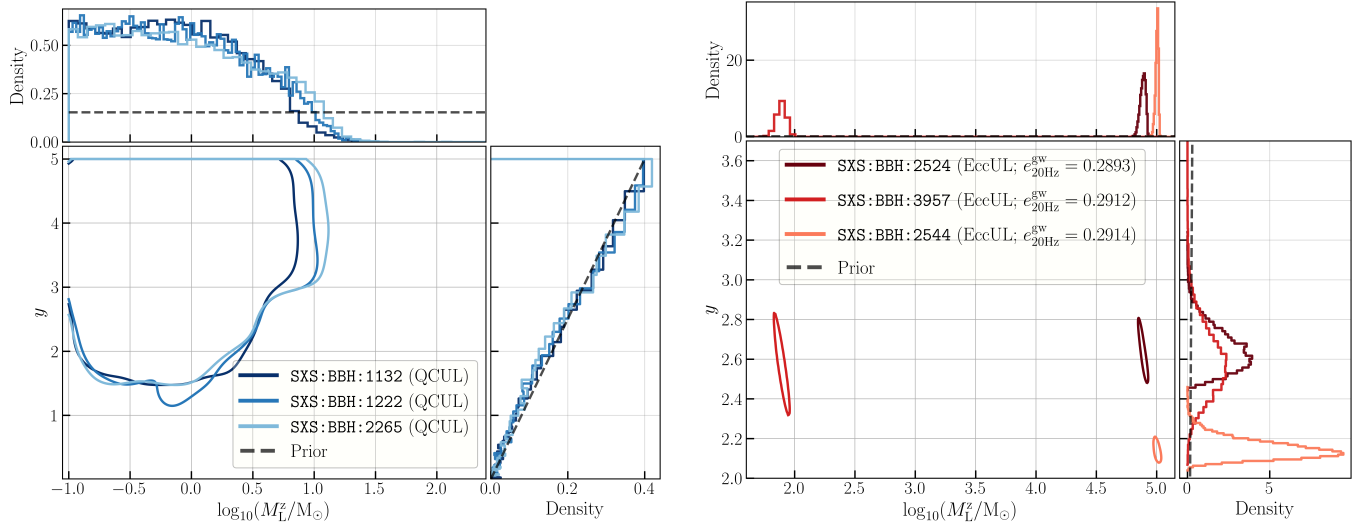


Figure 1: Inferred microlens parameters, $\log_{10} M_L^z$ and y , for three non-spinning QCUL NR injections (left panel) and three non-spinning EccUL NR injections (right panel), generated using SXS simulations (SXS IDs mentioned in the legend). The bottom-left subpanels display the inferred 1σ credible regions for the lens parameters, while the adjacent panels show the corresponding 1D marginalized posteriors. For eccentric simulations, we additionally report the gauge-independent eccentricity measured at 20 Hz ($e_{20\text{ Hz}}^{\text{gw}}$) using the `gw_eccentricity` package.

and the aligned spin components are allowed to vary in $[-0.9, 0.9]$ with a prior uniform in magnitude and isotropic in orientation (uniform in the cosine of the tilt angle). Rest of the priors are chosen to be agnostic and sufficiently wide around the true injected values. We use the same mode content to that used in the injections, and set the likelihood low-frequency cutoff $f_{\text{low}} = 20$ Hz. The sampling frequency is set to 2048 Hz. For the QCUL hypothesis, we adopt the same settings, except that both the eccentricity and anomaly parameters are fixed to zero. Since `TEOBResumS-Dali` is relatively slower waveform to evaluate ($\mathcal{O}(10^{-1}$ s) per waveform evaluation), we use `nlive` = 500 and relax the absolute and relative error tolerances of its ordinary differential equations (ODEs) integrator from their default values of 10^{-13} and 10^{-12} to 10^{-8} and 10^{-7} (see [112] for more details), respectively, reducing the evaluation cost to $\mathcal{O}(10^{-2})$ s per evaluation.

The resulting Bayes factors, listed in the final column of Table I, show that all eccentric injections yield $\log_{10} \mathcal{B}_{\text{QCUL}}^{\text{EccUL}} \gg 1$, indicating strong evidence for eccentricity. Conversely, quasicircular injections correctly show no support for eccentricity ($\log_{10} \mathcal{B}_{\text{QCUL}}^{\text{EccUL}} < 0$). Moreover, for all eccentric injections we find $\log_{10} \mathcal{B}_{\text{QCUL}}^{\text{EccUL}} \gg \log_{10} \mathcal{B}_{\text{QCUL}}^{\text{QCML}}$, demonstrating that eccentric models provide far better fits than microlensing models. This indicates that the degeneracy between eccentricity-induced and microlensing-induced waveform features is *weak* and can be broken when the correct waveform family is used in the analysis. This conclusion is further corroborated by the fact that, at lower network SNRs (e.g., SNR 15), we do not observe any significant support for the microlensing hypothesis ($\log_{10} \mathcal{B}_{\text{QCUL}}^{\text{QCML}} < 0$) when repeating the same exercise (although we do not explicitly present those

results here).

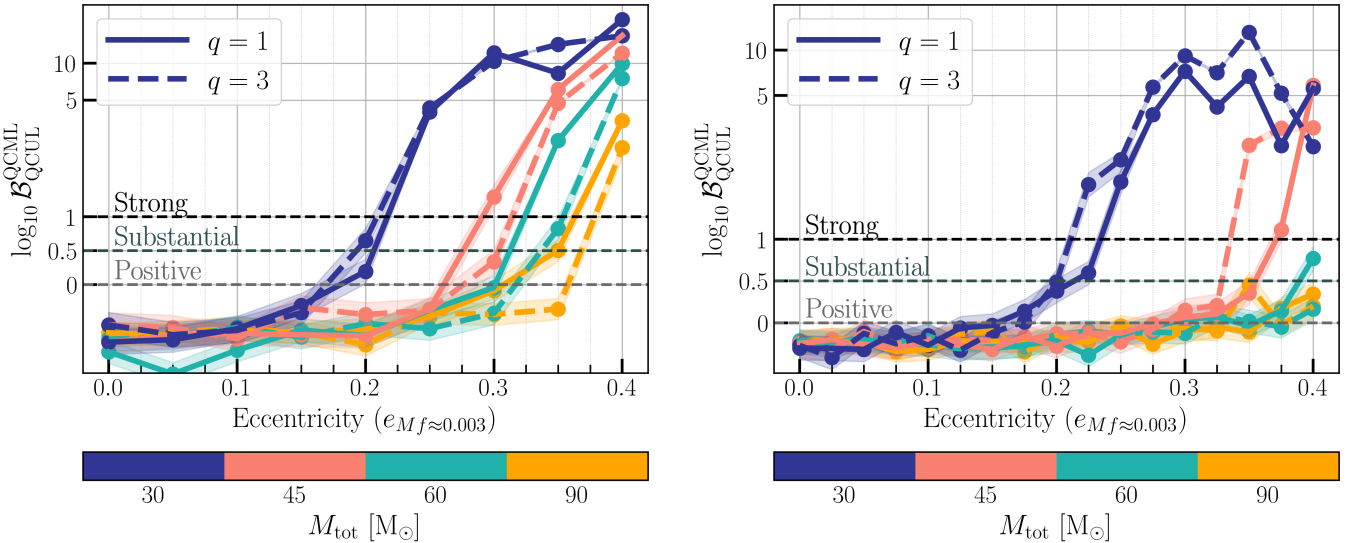
The findings in this section highlight the presence of degeneracies between the observational signatures of microlensing and eccentricity in GWs from a BBH system, underscoring the need for a more comprehensive investigation. We address this in the subsequent sections.

B. Injection Study using `TEOBResumS-Dali`

To explore the degeneracy over a broader region of parameter space of eccentricity, binary mass and the mass-ratio, we utilize `TEOBResumS-Dali` [105–111] waveform model to perform eccentric injections

For injections, we choose four distinct binary mass values $M_{\text{tot}}/M_{\odot} \in \{30, 45, 60, 90\}$, two mass ratio values $q \in \{1, 3\}$, and eccentricity (e) values sampled as follows: for analyses using `IMRPhenomXPHM-SpinTaylor`, e ranges from 0 to 0.4 in steps of 0.025, while for `TEOBResumS-Dali`, e ranges from 0 to 0.4 in steps of 0.05. This choice is made because, as mentioned in Sec. III A, `TEOBResumS-Dali` is typically slower to evaluate than `IMRPhenomXPHM-SpinTaylor`. These eccentricity values are defined at a dimensionless apastron frequency of $M f_{\text{ref}} \approx 0.003$ evaluated for the fundamental ($\ell = 2, |m| = 2$) mode at apastron, which corresponds to 10 Hz for a $60 M_{\odot}$ BBH system⁷. This ensures that we define eccentricity at the same point in

⁷ We choose this value because according to Table I of [113], `TEOBResumS-Dali` has been shown to be faithful against NR simulations up to an eccentricity of ~ 0.3 at 10 Hz for a $60 M_{\odot}$ BBH system.



(a) Bayesian model comparison between QCML and QCUL hypotheses performed using the `TEOBResumS-Dali` waveform model, where in-plane spin components, eccentricity, and the true anomaly are fixed to zero during inference.

(b) Bayesian model comparison between QCML and QCUL hypotheses using the `IMRPhenomXPHM-SpinTaylor` waveform approximant, where all 15 parameters are utilized during inference.

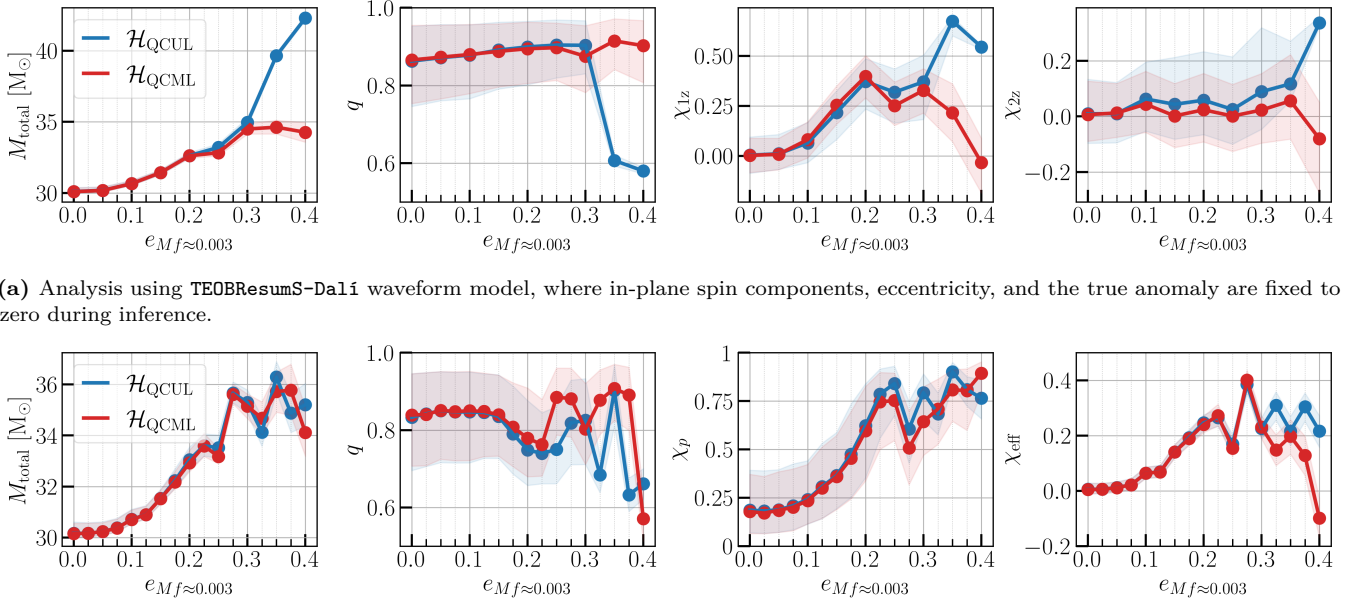
Figure 2: Bias in microlensing searches arising from the presence of eccentricity in the signal. The variation in the Bayes factors between the QCML and QCUL hypotheses, $\log_{10} \mathcal{B}_{\text{QCML}}^{\text{QCML}}$, is shown as a function of the eccentricity (e) (x-axis), total binary mass (M_{tot}) (color scale), and mass ratio (q) (solid vs. dashed lines). Eccentricity is defined at a dimensionless frequency of ~ 0.003 at apastron. The uncertainty in the estimated $\log_{10} \mathcal{B}_{\text{QCML}}^{\text{QCML}}$ is represented by the translucent bands around each curve. The injections are performed using the `TEOBResumS-Dali` waveform model, while the recovery (evidence computation) is done using two different quasicircular models: (a) `TEOBResumS-Dali` with eccentricity and related parameters fixed to zero, and (b) `IMRPhenomXPHM-SpinTaylor` allowing all 15 parameters to vary. These results demonstrate that neglecting eccentricity in waveform modeling can lead to spurious support for the microlensing hypothesis, especially at higher eccentricities.

the evolution of a binary. We consider only $(\ell, |m|) = \{(2, 2), (2, 1), (3, 2), (3, 3), (4, 4)\}$ modes for the injection. The luminosity distance is adjusted to produce a true network optimal SNR of 30 for each injection. Other extrinsic parameters are set to the median posterior values inferred for GW150914 [101]. We note that ideally one should utilize full signal content above $f_{\text{low}} = 20$ Hz, which implies considering the signal from the point when its periastron frequency of the fundamental mode crosses $f_{\text{start}} = f_{\text{low}} \cdot (2/m_{\text{max}}) = 10$ Hz, where m_{max} corresponds to the largest m among all included modes (see Eq. 18 in [98]), as we did in the last section III A. However, in this section, we consider the waveform from the point when the apastron frequency of the fundamental mode crosses f_{ref} .⁸ We do this mainly to decrease computational expense. If we had instead started the waveform at the point where the periastron frequency crosses f_{ref} , then both the waveform duration and the waveform evaluation time would increase with eccentricity, making PE runs significantly costlier.

1. Inference with quasicircular templates for Eccentric Injections

To isolate the effect of ignoring eccentricity in microlensing searches, we first analyze the signals using the quasicircular, aligned-spin version of the `TEOBResumS-Dali` waveform model, thereby avoiding possible waveform systematics. In this setup, the in-plane spin components, eccentricity, and true anomaly are all fixed to zero. The injected signals and the recovery analysis employ identical mode content. The corresponding results are shown in Fig. 2a. First, we observe that the degeneracy between eccentricity-induced and microlensing-induced waveform features, as quantified by the Bayes factor $\log_{10} \mathcal{B}_{\text{QCML}}^{\text{QCML}}$, increases almost monotonically with eccentricity across all binary masses considered. At the highest eccentricity value investigated, $e_{Mf \approx 0.003} = 0.4$, $\mathcal{H}_{\text{QCML}}$ is very strongly favored over $\mathcal{H}_{\text{QCUL}}$, with $\log_{10} \mathcal{B}_{\text{QCML}}^{\text{QCML}} > 1$ for all binary masses and mass ratios. Second, the degeneracy is stronger for lighter binaries and weakens with increasing total mass (maximum for the purple curves and minimum for the orange ones). This suggests that degeneracy increases with increasing number of GW cycles, which is expected. Third, we do not find any significant difference in $\log_{10} \mathcal{B}_{\text{QCML}}^{\text{QCML}}$ between the two mass-ratio cases

⁸ In `TEOBResumS-Dali`, the reference frequency f_{ref} where the eccentricity is defined and the starting frequency f_{start} of the fundamental mode are same.



(a) Analysis using **TEOBResumS-Dalí** waveform model, where in-plane spin components, eccentricity, and the true anomaly are fixed to zero during inference.

(b) Analysis using **IMRPhenomXPHM-SpinTaylor** waveform approximant, where all 15 parameters are varied during inference.

Figure 3: Comparison of the inferred intrinsic parameters as a function of eccentricity ($e_{Mf} \approx 0.003$) when eccentric injections are analyzed under the quasicircular microlensed (QCML; \mathcal{H}_{QCML}) and quasicircular unlensed (QCUL; \mathcal{H}_{QCUL}) hypotheses. For the **TEOBResumS-Dalí** waveform model [panel (a)], the intrinsic parameters shown are the total mass (M_{tot}), mass ratio (q), and aligned spin components (χ_{1z}, χ_{2z}). For the **IMRPhenomXPHM-SpinTaylor** model [panel (b)], we instead show the total mass (M_{tot}), mass ratio (q), effective precession spin parameter (χ_p), and effective aligned-spin parameter (χ_{eff}). All results correspond to non-spinning injections with $\{M_{\text{tot}} = 30 \text{ M}_\odot, q = 1\}$. The points denote the median values of the one-dimensional marginalized posteriors, and the shaded bands indicate the corresponding 1σ uncertainties. In panel (a), in-plane spins, eccentricity, and true anomaly are fixed to zero during inference, whereas in panel (b), all 15 parameters are varied.

considered.

The degeneracy between the observational signatures of eccentricity and microlensing can be further understood by examining how well \mathcal{H}_{QCML} performs relative to \mathcal{H}_{QCUL} in recovering the injected parameters. In Fig. 3a, we show the recovered intrinsic parameters: total mass (M_{tot}), mass ratio (q), and the aligned spin components (χ_{1z}, χ_{2z}). We show this comparison only for the $\{M_{\text{tot}} = 30 \text{ M}_\odot, q = 1\}$ case, which corresponds to one of the configurations that led to the largest biases in microlensing searches, as seen in Fig. 2a. For all parameters, we find that the biases in the recovered values remain broadly consistent between \mathcal{H}_{QCML} and \mathcal{H}_{QCUL} up to $e \sim 0.2$, but start diverging at higher eccentricities. Overall, the biases are comparable or smaller for \mathcal{H}_{QCML} than for \mathcal{H}_{QCUL} , indicating that microlensing can mimic eccentric features well enough to yield more accurate intrinsic parameter recovery, further reinforcing the degeneracy between eccentric and microlensed GW signals.

Motivated by ongoing searches for microlensing signatures using Bayesian model comparison, we also analyze the injections with the quasicircular unlensed waveform model **IMRPhenomXPHM-SpinTaylor** [102–104, 114], a fully precessing model that employs all 15 parameters to describe a typical QCUL BBH waveform, including

higher-order modes. The injected signals and recovery analyses use the same mode content. The results are shown in Fig. 2b. Here, we again observe a similar trend in $\log_{10} \mathcal{B}_{QCUL}^{QCML}$ as a function of eccentricity and total binary mass, an almost monotonic increase with eccentricity and stronger degeneracy for lower masses. However, for the $M_{\text{tot}} = 30 \text{ M}_\odot$ case, $\log_{10} \mathcal{B}_{QCUL}^{QCML}$ rises to $\gtrsim 8$ at $e = 0.3$ and then starts to oscillate, deviating from the monotonic behavior. This deviation can be attributed to primarily three factors. First, since we consider signals starting from the time when the apastron frequency of the dominant $(\ell, |m|) = (2, 2)$ mode crosses the starting frequency f_{start} , the duration of our injected signals decrease with increasing eccentricity values. This trend is opposite to what would occur in a more realistic setup where signals should ideally start from the time when the periastron frequency crosses f_{start} . Consequently, in our configuration, the number of GW cycles decreases with increasing eccentricity, and we therefore do not expect $\log_{10} \mathcal{B}_{QCUL}^{QCML}$ to increase monotonically with e . Second, the degeneracy between eccentricity and the intrinsic parameters, particularly the precession, also becomes important, as illustrated in Fig. 3b. There, we show the inferred intrinsic parameters (from left to right): the total mass (M_{tot}), mass ratio (q), effective precession spin parameter (χ_p), and effective aligned-spin parameter (χ_{eff}).

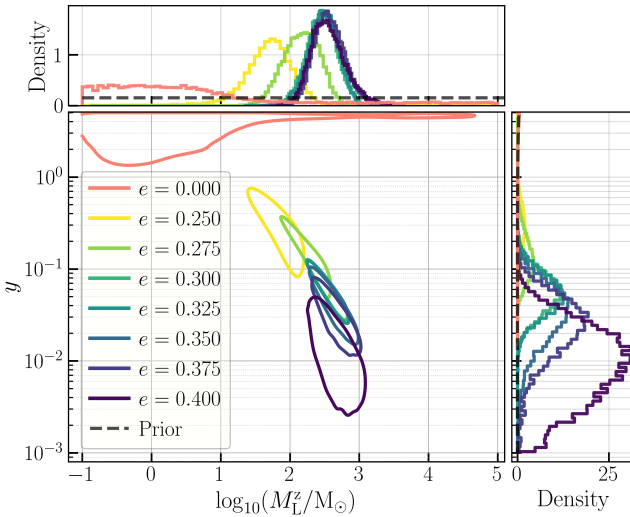


Figure 4: Inferred microlens parameters, $\log_{10} M_L^z$ and y , for non-spinning eccentric injections with $\{M_{\text{tot}} = 30 \text{ M}_\odot, q = 1\}$, analyzed using `IMRPhenomXPHM-SpinTaylor`. We show results only for cases with $\log_{10} \mathcal{B}_{\text{QCUL}}^{\text{QCML}} > 1$, with the $e = 0$ case included for reference. The bottom-left panel displays the inferred 1σ credible regions for the lens parameters, while the adjacent panels show the corresponding one-dimensional marginalized posteriors.

As evident from the figure, there exists a significant degeneracy between eccentricity and precession, as well as between eccentricity and the total mass, consistent with previous studies [69, 115–121]. The oscillations in the inferred parameters could be one of the reasons for the oscillations seen in $\log_{10} \mathcal{B}_{\text{QCUL}}^{\text{QCML}}$. Additionally, unlike in Fig. 3a, the biases in the inferred parameters are not always smaller for $\mathcal{H}_{\text{QCML}}$ than for $\mathcal{H}_{\text{QCUL}}$. Due to this degeneracy between eccentricity and the precession, the Bayes factors in case of `IMRPhenomXPHM-SpinTaylor` are always lower than that of `TEOBResumS-Dali` for cases with $\log_{10} \mathcal{B}_{\text{QCUL}}^{\text{QCML}} > 1$. Third, even if we assume that the degeneracy between microlensing and eccentric features increases monotonically with eccentricity, we should still not expect $\log_{10} \mathcal{B}_{\text{QCUL}}^{\text{QCML}}$ to increase monotonically with e . This is because the prior on y favors larger values, where microlensing effects are weak (see Eq. 3). Since the evidence depends sensitively on the prior volume, the stronger microlensing features at low y are down-weighted by the prior. As a result, the combined effect could lead to a non-monotonic behavior of $\log_{10} \mathcal{B}_{\text{QCUL}}^{\text{QCML}}$ as a function of eccentricity.

For $\{M_{\text{tot}} = 30 \text{ M}_\odot, q = 1\}$ injections analyzed with `IMRPhenomXPHM-SpinTaylor`, the inferred 1σ credible regions for the lens parameters, M_L^z and y , are shown in Fig. 4 for all cases with $\log_{10} \mathcal{B}_{\text{QCUL}}^{\text{QCML}} > 1$, with the $e = 0$ case included for reference. As seen in the figure, for all cases where the evidence favors $\mathcal{H}_{\text{QCML}}$, the posteriors for the lens parameters are well localized. The inferred M_L^z values typically lie in the range $\sim 10\text{--}10^3 \text{ M}_\odot$. Further-

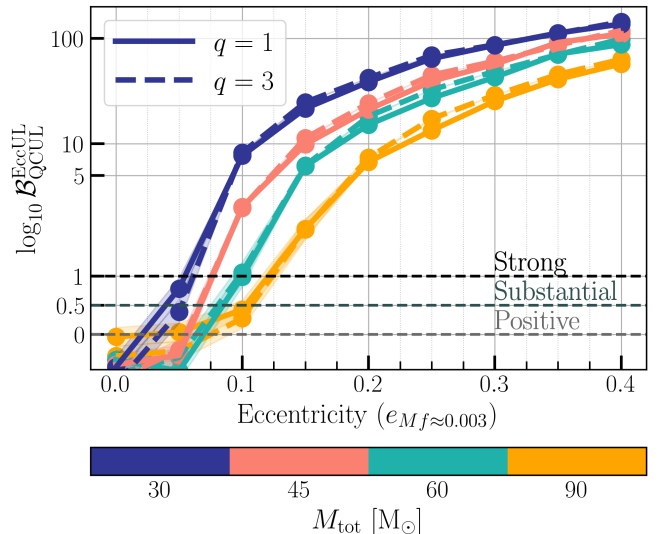


Figure 5: Variation in the Bayes factors between the EccUL and QCUL hypotheses, $\log_{10} \mathcal{B}_{\text{QCUL}}^{\text{EccUL}}$, shown as a function of the eccentricity (e) (x-axis), total binary mass (M_{tot}) (color scale), and mass ratio (q) (solid vs. dashed lines). Eccentricity is defined at a dimensionless frequency of ~ 0.003 at apastron. The uncertainty in the estimated Bayes factors are represented by the translucent bands around each curve.

more, the inferred y decreases with increasing eccentricity. All these contours differ significantly from those obtained for a truly quasicircular injection (salmon-colored contour).

In this section, we have demonstrated that neglecting eccentricity can introduce significant biases when searching for microlensing signatures in GW signals from BBH systems. Our results also suggest that the interplay among precession, eccentricity, and microlensing may impact the analysis in a complex manner. Next, we investigate whether this degeneracy can be mitigated by employing waveform models consistent with the injections, that is, by doing the inference using eccentric waveform models.

2. Breaking the Degeneracy: Eccentric Inference for Eccentric Injections

In this section, we investigate whether the degeneracy between eccentricity-induced and microlensing-induced features can be broken when analyzing eccentric injections with eccentric templates, i.e., templates that include all relevant physical effects present in the injections.

We analyze the injections using the `TEOBResumS-Dali` waveform model under the EccUL hypothesis, which is the same model used for the injections. The eccentricity is treated as a free parameter with a uniform prior in $[0, 0.45]$, defined at the apastron frequency, which is set equal to the waveform starting frequency of $f_{\text{start}} = 10 \text{ Hz}$. The true anomaly and the in-plane spin components are fixed to zero, while the aligned spin components vary in

$[-0.9, 0.9]$ with a prior uniform in magnitude and isotropic in orientation (uniform in the cosine of the tilt angle). All remaining priors are chosen to be agnostic and sufficiently broad around the true injected values. We employ the same mode content used in the injections and set the likelihood low-frequency cutoff to $f_{\text{low}} = 20$ Hz. The sampling frequency is 2048 Hz. All other settings are kept consistent with those used for the EccUL analysis in Sec. III A.

The results are shown in Fig. 5, where we display the Bayes factors between the EccUL and QCUL hypotheses, $\log_{10} \mathcal{B}_{\text{QCUL}}^{\text{EccUL}}$. We first observe that $\log_{10} \mathcal{B}_{\text{QCUL}}^{\text{EccUL}}$ increases monotonically with eccentricity across all $\{M_{\text{tot}}, q\}$ configurations considered. Comparing these values with the corresponding $\log_{10} \mathcal{B}_{\text{QCUL}}^{\text{QCML}}$ in Fig. 2a, we find that the former becomes an order of magnitude larger than the latter for $e \gtrsim 0.05$. This demonstrates that the degeneracy between eccentricity and microlensing can indeed be broken when the analysis employs waveform models that correctly capture all relevant physics of the signal, namely eccentricity, preventing erroneous claims of microlensing.

IV. CONCLUSION

In this work, we investigated the extent to which orbital eccentricity in BBH GW signals can mimic the observational signatures of microlensing produced by an isolated point-mass lens, potentially leading to false claims of microlensing. Using a combination of highly reliable NR simulations, TEOBResumS-Dali eccentric injections, and Bayesian model comparison analyses, supported by a complementary mismatch study across a simulated eccentric BBH population, we assessed when this degeneracy becomes significant and whether it can be resolved by including eccentric waveform models in the recovery.

Our main conclusions are as follows:

1. Bayesian model comparison analyses of both NR and TEOBResumS-Dali EccUL injections demonstrate that ignoring eccentricity can bias microlensing searches in certain regions of the parameter space. Specifically, this degeneracy strengthens with (i) increasing eccentricity, (ii) decreasing total mass, and (iii) increasing SNR. Consequently, $\mathcal{H}_{\text{QCML}}$ can be strongly favored over $\mathcal{H}_{\text{QCUL}}$ under these conditions, even when the true signal is not microlensed.
2. For NR injections with a gauge-independent eccentricity measured at 20 Hz to be $e_{20 \text{ Hz}}^{\text{gw}} \sim 0.3$, total mass $M_{\text{tot}} \approx 80 M_{\odot}$, and mass ratios $q \in \{1, 2, 3\}$, we find that the $\mathcal{H}_{\text{QCML}}$ is very strongly preferred over the $\mathcal{H}_{\text{QCUL}}$, yielding $\log_{10} \mathcal{B}_{\text{QCUL}}^{\text{QCML}} \gtrsim 10$, when the true injected optimal network SNR is around 100. In contrast, no such bias appears for lower-SNR injections (~ 15), for which $\log_{10} \mathcal{B}_{\text{QCUL}}^{\text{QCML}} < 0$ across all eccentric injections.

3. For a network optimal SNR of 30, binaries with $M_{\text{tot}} \lesssim 100 M_{\odot}$ and high eccentricities ($\gtrsim 0.4$, defined at apastron at $Mf \approx 0.003$), almost always favor the $\mathcal{H}_{\text{QCML}}$, having $\log_{10} \mathcal{B}_{\text{QCUL}}^{\text{QCML}} \gtrsim 1$.
4. In cases where the $\mathcal{H}_{\text{QCML}}$ is strongly favored over the $\mathcal{H}_{\text{QCUL}}$, the inferred microlens parameters, $\log_{10} M_{\text{L}}^z$ and y , exhibit well-localized posteriors and large Jensen-Shannon divergence values between the priors and the inferred 1D marginalized posteriors for the lens parameters.
5. Since $\mathcal{H}_{\text{QCUL}}$ is a subset of $\mathcal{H}_{\text{QCML}}$ (because microlensing effects are added on top of the unlensed waveform, in the weak microlensing regime both hypotheses produce similar, or *faithful*, signals), we expect $\mathcal{H}_{\text{QCML}}$ to perform at least as well as $\mathcal{H}_{\text{QCUL}}$ when the true signal is EccUL (or, more generally, when any physics is missing from the model). However, introducing additional parameters in $\mathcal{H}_{\text{QCML}}$ also incurs a penalty owing to *Occam's razor*, which suppresses false microlensing support except in the regimes identified above.
6. For both NR and TEOBResumS-Dali EccUL injections, the degeneracy is always broken when the recovery uses eccentric templates containing the correct physics. In such cases, $\log_{10} \mathcal{B}_{\text{QCUL}}^{\text{EccUL}} \gg \log_{10} \mathcal{B}_{\text{QCUL}}^{\text{QCML}}$, typically by an order of magnitude. Thus, events which are prone to showing strong, but spurious, support for microlensing are expected to show even greater support for eccentricity when recovered with an appropriate eccentric waveform model. Thus, the degeneracy is not intrinsic to the signal: it reflects an incomplete model space rather than any physical ambiguity.

The findings suggest that although $\mathcal{H}_{\text{QCML}}$ can be strongly favored over the $\mathcal{H}_{\text{QCUL}}$, it occurs only when either the signal is strongly eccentric or has a high enough SNR. The broader implications of this degeneracy are twofold. First, any event showing strong evidence for microlensing under a quasicircular model must be subjected to a parallel analysis using eccentric waveform families. Only if the microlensing hypothesis remains preferred once eccentricity is allowed can a physical lens interpretation be considered robust. Second, since the effects of non-zero eccentricity become increasingly important when probing earlier stages of binary evolution or with improved detector sensitivities, our results carry important implications for future observatories such as third-generation detectors (CE, ET) and space-based missions like DECIGO and LISA. At lower frequencies, eccentric modulations persist for more cycles and can more readily imitate the diffraction patterns of microlensing, while higher SNRs will make any spurious preference statistically more significant.

However, we emphasize that many astrophysical formation channels that produce substantial eccentricities, including dynamical interactions and hierarchical

triples, often generate significant in-plane spins and hence strong precession. The current lack of *faithful* precessing-eccentric waveform models may, therefore, pose challenges to fully breaking this degeneracy in realistic analyses. In such scenarios, models incorporating both microlensing and precession may outperform aligned-spin eccentric models. We will explore this interesting line of investigation in our future work.

Our findings highlight a clear prescription for microlensing searches: strong Bayesian support for microlensing under quasicircular models does not guarantee a physical lensing event, and must always be tested for other *atypical* physical effects, such as eccentricity, to ensure unbiased, astrophysically reliable interpretation in the era of precision GW astronomy. Finally, while we focused here primarily on biases in microlensing searches introduced by ignoring non-zero eccentricity, the converse possibility is equally important: biases in eccentricity searches induced by microlensing or other atypical physical effects. Such degeneracies may be resolved by analyzing the evolution of the inferred eccentricity as a function of frequency and assessing its consistency with post-Newtonian predictions [122]. Investigating such reverse degeneracies will further clarify the robustness of eccentricity inference in future GW observations.

ACKNOWLEDGMENTS

We sincerely thank Nathan K. Johnson-McDaniel for many useful discussions during the early phase of this project. We also thank Akash Maurya for many useful comments and discussions, and Aditya Vijaykumar for carefully reading the manuscript. We would also like to thank P. Ajith, Sukanta Bose, Anuradha Gupta, Shasvath Kapadia, Prayush Kumar, Paul Lasky, Anupreeta More, Purnima Narayan, Anirudh S. Nemmani, Archana Pai, Arif Shaikh, and Aditya Sharma for their useful comments and questions. The authors are grateful for computational resources provided by the LIGO Laboratory and supported by National Science Foundation Grants PHY-0757058 and PHY-0823459. We also acknowledge the use of the IUCAA LDG cluster Sarathi for computational work.

The work utilizes the following software packages: Cython [123], NumPy [124], SciPy [125], PyCBC [126], LALSuite [127], dynesty [96], Bilby [94, 95], PEsummary [128], gw_eccentricity [98, 100], GWPopulation [129], Matplotlib [130], and Jupyter notebook [131].

Appendix A: Microlensing biases for an Eccentric BBH Population using Mismatch Analysis

To understand the broader impact of eccentricity on microlensing searches, we study a population of eccentric BBH signals. We generate mock GW data of around

$\sim 2 \times 10^4$ non-spinning eccentric BBH signals using `TEOBResumS-Dali` [105–111] waveform model. The mass and spin priors are derived from the inferred population model based on GWTC-3 data [132]: the source-frame component masses are drawn from the POWER-LAW+PEAK distribution, and spins are assumed to be independent and identically distributed, with magnitudes following a Beta distribution and tilt angles modeled as an isotropic plus truncated half-Gaussian mixture [133]. The merger rate density follow the Madau–Dickinson profile [134, 135], with cosmological parameters taken from with [136]. For simplicity, we only consider one detector (Hanford LIGO detector) for this study, and consider only those signals that have an SNR above 8. The noise PSD correspond to the target O4 LIGO sensitivity. We define eccentricities at a fixed point in the binary evolution by imposing a dimensionless frequency of ~ 0.003 at apastron, equivalent to 10 Hz for a $60 M_\odot$ BBH. The eccentricity prior is log-uniform over $e \in (0.01, 0.5)$.

Our goal is to compare the performance of $\mathcal{H}_{\text{QCUL}}$ and $\mathcal{H}_{\text{QCML}}$ when analyzing eccentric signals. Since computing evidences with a nested sampler is computationally expensive, we utilize Laplace’s approximation as used in Eq. 26 of [137] (neglecting the Occam factor) to approximate the Bayes factor of a hypothesis \mathcal{H} against the noise-only hypothesis:

$$\ln \mathcal{B}_{\text{noise}}^{\mathcal{H}} \approx \frac{\rho_{\mathcal{H}}^2}{2} \quad (\text{A1})$$

Thus, $\ln \mathcal{B}_{\text{QCUL}}^{\text{QCML}}$ can be estimated as:

$$\begin{aligned} \ln \mathcal{B}_{\text{QCUL}}^{\text{QCML}} &= \ln \mathcal{B}_{\text{noise}}^{\text{QCML}} - \ln \mathcal{B}_{\text{noise}}^{\text{QCUL}} \\ &= \frac{1}{2}(\rho_{\mathcal{H}_{\text{QCML}}}^2 - \rho_{\mathcal{H}_{\text{QCUL}}}^2) \\ &= \frac{1}{2}(FF_{\text{QCML}}^2 - FF_{\text{QCUL}}^2)\rho_{\text{EccUL}}^2 \end{aligned} \quad (\text{A2})$$

where FF_{QCUL} (FF_{QCML}) are the fitting factor (FF) values when QCUL (QCML) model is used to analyze the EccUL target waveforms, and ρ_{EccUL} depicts the true optimal SNR of the eccentric signal. In writing this, we used the relation $\rho_{\text{EccUL}} = \rho_{\text{QCUL}}/FF_{\text{QCUL}} = \rho_{\text{QCML}}/FF_{\text{QCML}}$ [138]. We use `TEOBResumS-Dali` for computing *match* values, with the lower and upper frequency cutoffs set to 20 Hz and 1024 Hz, respectively. To compute the FF values, we use the Nelder-Mead algorithm [139], as implemented in the `optimization` module of the `Scipy` library [125], to maximize the *match* between the waveforms (for more details, see Sec. 2.2 of [62]). For $\mathcal{H}_{\text{QCUL}}$, we employ a 4D aligned-spin waveform (WF) model to analyze the eccentric WFs, parameterized by: chirp mass (\mathcal{M}_c), mass ratio (q), and aligned spin components of the two component masses (χ_{1z} , χ_{2z}). For $\mathcal{H}_{\text{QCML}}$, we use a 6D WF model with two additional parameters than that in $\mathcal{H}_{\text{QCUL}}$, namely, $\log_{10} M_L^z$ and y . All remaining parameters are fixed to their true values. Since we maximize over continuous parameters, our FF computation does not include additional loss from

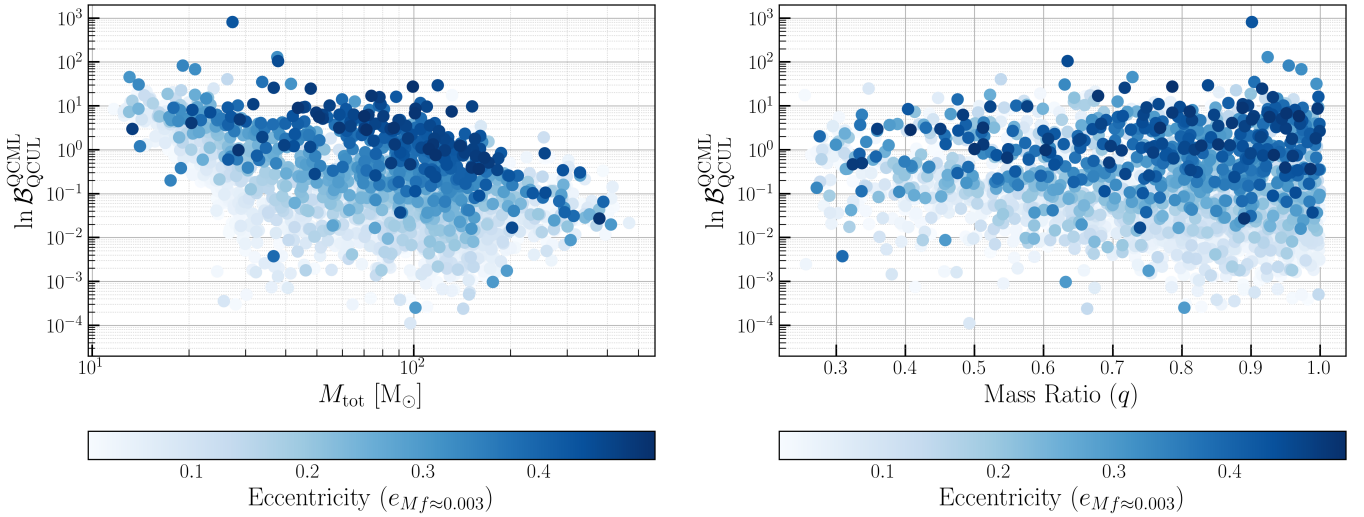


Figure 6: $\ln \mathcal{B}_{\text{QCUL}}^{\text{QCML}}$ estimated from fitting factor differences using Eq. A2 for the simulated eccentric BBH population, plotted against total mass M_{total} (left) and mass ratio q (right). The color bar denotes eccentricity ($e_{Mf \approx 0.003}$). $\ln \mathcal{B}_{\text{QCUL}}^{\text{QCML}}$ increases with eccentricity, shows a slight anti-correlation with total mass, and exhibits no significant trend with mass ratio.

a discrete *template bank*; we isolate only the loss due to *missing physics* in the waveform models used for the inference.

In Fig. 6, we show $\ln \mathcal{B}_{\text{QCUL}}^{\text{QCML}}$ for our simulated eccentric BBH population against the total binary mass (left panel) and mass ratio (right panel), with color bar representing eccentricity values. We observe: (i) For any value on the x-axis, the $\ln \mathcal{B}_{\text{QCUL}}^{\text{QCML}}$ increases with increasing eccentricity values (i.e., the points transition from lighter

to darker shades as the y-values rise); (ii) For a fixed eccentricity value, the left panel of Fig. 6 shows a mild anti-correlation between $\ln \mathcal{B}_{\text{QCUL}}^{\text{QCML}}$ and the total binary mass M_{total} ; and (iii) the right panel of Fig. 6 shows no significant correlation between $\ln \mathcal{B}_{\text{QCUL}}^{\text{QCML}}$ and q .

Overall, the fitting factor analysis presented in this section is consistent with the full Bayesian model-comparison results of Sec. III.

[1] J. Aasi *et al.* (LIGO Scientific), *Class. Quant. Grav.* **32**, 074001 (2015), [arXiv:1411.4547 \[gr-qc\]](https://arxiv.org/abs/1411.4547).

[2] F. Acernese *et al.* (VIRGO), *Class. Quant. Grav.* **32**, 024001 (2015), [arXiv:1408.3978 \[gr-qc\]](https://arxiv.org/abs/1408.3978).

[3] K. Somiya (KAGRA), *Class. Quant. Grav.* **29**, 124007 (2012), [arXiv:1111.7185 \[gr-qc\]](https://arxiv.org/abs/1111.7185).

[4] Y. Aso, Y. Michimura, K. Somiya, M. Ando, O. Miyakawa, T. Sekiguchi, D. Tatsumi, and H. Yamamoto (KAGRA), *Phys. Rev. D* **88**, 043007 (2013), [arXiv:1306.6747 \[gr-qc\]](https://arxiv.org/abs/1306.6747).

[5] T. Akutsu *et al.* (KAGRA), *Nature Astron.* **3**, 35 (2019), [arXiv:1811.08079 \[gr-qc\]](https://arxiv.org/abs/1811.08079).

[6] T. Akutsu *et al.* (KAGRA), *PTEP* **2021**, 05A101 (2021), [arXiv:2005.05574 \[physics.ins-det\]](https://arxiv.org/abs/2005.05574).

[7] B. P. Abbott *et al.* (LIGO Scientific, Virgo), *Phys. Rev. X* **9**, 031040 (2019), [arXiv:1811.12907 \[astro-ph.HE\]](https://arxiv.org/abs/1811.12907).

[8] R. Abbott *et al.* (LIGO Scientific, Virgo), *Phys. Rev. X* **11**, 021053 (2021), [arXiv:2010.14527 \[gr-qc\]](https://arxiv.org/abs/2010.14527).

[9] R. Abbott *et al.* (LIGO Scientific, VIRGO), *Phys. Rev. D* **109**, 022001 (2024), [arXiv:2108.01045 \[gr-qc\]](https://arxiv.org/abs/2108.01045).

[10] R. Abbott *et al.* (KAGRA, VIRGO, LIGO Scientific), *Phys. Rev. X* **13**, 041039 (2023), [arXiv:2111.03606 \[gr-qc\]](https://arxiv.org/abs/2111.03606).

[11] A. G. Abac *et al.* (LIGO Scientific, VIRGO, KAGRA), [arXiv:2508.18082](https://arxiv.org/abs/2508.18082) (2025), [arXiv:2508.18082 \[gr-qc\]](https://arxiv.org/abs/2508.18082).

[12] M. Punturo *et al.*, *Class. Quant. Grav.* **27**, 194002 (2010).

[13] S. Hild *et al.*, *Class. Quant. Grav.* **28**, 094013 (2011), [arXiv:1012.0908 \[gr-qc\]](https://arxiv.org/abs/1012.0908).

[14] D. Reitze *et al.*, *Bull. Am. Astron. Soc.* **51**, 035 (2019), [arXiv:1907.04833 \[astro-ph.IM\]](https://arxiv.org/abs/1907.04833).

[15] B. P. Abbott *et al.* (LIGO Scientific), *Class. Quant. Grav.* **34**, 044001 (2017), [arXiv:1607.08697 \[astro-ph.IM\]](https://arxiv.org/abs/1607.08697).

[16] T. Regimbau, M. Evans, N. Christensen, E. Katsavounidis, B. Sathyaprakash, and S. Vitale, *Phys. Rev. Lett.* **118**, 151105 (2017), [arXiv:1611.08943 \[astro-ph.CO\]](https://arxiv.org/abs/1611.08943).

[17] P. Amaro-Seoane *et al.*, [arXiv:1702.00786](https://arxiv.org/abs/1702.00786) (2017), [arXiv:1702.00786 \[astro-ph.IM\]](https://arxiv.org/abs/1702.00786).

[18] S. Kawamura *et al.*, *Class. Quant. Grav.* **23**, S125 (2006).

[19] A. Einstein, *Science* **84**, 506 (1936).

[20] F. Zwicky, *Phys. Rev.* **51**, 290 (1937).

[21] D. Walsh, R. F. Carswell, and R. J. Weymann, *Nature* **279**, 381 (1979).

[22] G. Soucail, Y. Mellier, B. Fort, G. Mathez, and M. Cailloux, *Astronomy and Astrophysics* **191**, L19 (1988).

[23] O. A. Hannuksela, K. Haris, K. K. Y. Ng, S. Kumar, A. K. Mehta, D. Keitel, T. G. F. Li, and P. Ajith, *Astrophys. J. Lett.* **874**, L2 (2019), [arXiv:1901.02674 \[gr-qc\]](https://arxiv.org/abs/1901.02674).

[24] R. Abbott *et al.* (LIGO Scientific, VIRGO), *Astrophys. J.* **923**, 14 (2021), [arXiv:2105.06384 \[gr-qc\]](https://arxiv.org/abs/2105.06384).

[25] R. Abbott *et al.* (LIGO Scientific, KAGRA, VIRGO), *Astrophys. J.* **970**, 191 (2024), [arXiv:2304.08393 \[gr-qc\]](https://arxiv.org/abs/2304.08393).

[26] L. Dai, B. Zackay, T. Venumadhav, J. Roulet, and M. Zal-

darriaga, arXiv:2007.12709 (2020), arXiv:2007.12709 [astro-ph.HE].

[27] X. Liu, I. Magana Hernandez, and J. Creighton, *Astrophys. J.* **908**, 97 (2021), arXiv:2009.06539 [astro-ph.HE].

[28] J. Janquart *et al.*, *Mon. Not. Roy. Astron. Soc.* **526**, 3832 (2023), arXiv:2306.03827 [gr-qc].

[29] S. Mukherjee, B. D. Wandelt, and J. Silk, *Mon. Not. Roy. Astron. Soc.* **494**, 1956 (2020), arXiv:1908.08951 [astro-ph.CO].

[30] S. Goyal, K. Haris, A. K. Mehta, and P. Ajith, *Phys. Rev. D* **103**, 024038 (2021), arXiv:2008.07060 [gr-qc].

[31] T. Baker and M. Trodden, *Phys. Rev. D* **95**, 063512 (2017), arXiv:1612.02004 [astro-ph.CO].

[32] K. Liao, X.-L. Fan, X.-H. Ding, M. Biesiada, and Z.-H. Zhu, *Nature Commun.* **8**, 1148 (2017), [Erratum: *Nature Commun.* 8, 2136 (2017)], arXiv:1703.04151 [astro-ph.CO].

[33] S. Jana, S. J. Kapadia, T. Venumadhav, and P. Ajith, *Phys. Rev. Lett.* **130**, 261401 (2023), arXiv:2211.12212 [astro-ph.CO].

[34] S. Mukherjee, T. Broadhurst, J. M. Diego, J. Silk, and G. F. Smoot, *Mon. Not. Roy. Astron. Soc.* **506**, 3751 (2021), arXiv:2106.00392 [gr-qc].

[35] O. A. Hannuksela, T. E. Collett, M. Çalışkan, and T. G. F. Li, *Mon. Not. Roy. Astron. Soc.* **498**, 3395 (2020), arXiv:2004.13811 [astro-ph.HE].

[36] J. K. Lawrence, *Nuovo Cimento B Serie 6B*, 225 (1971).

[37] H. C. Ohanian, *Int. J. Theor. Phys.* **9**, 425 (1974).

[38] F. Bernardeau, arXiv:astro-ph/9901117 (1999), arXiv:astro-ph/9901117.

[39] R. Takahashi, *Astrophys. J.* **835**, 103 (2017), arXiv:1606.00458 [astro-ph.CO].

[40] L. Dai and T. Venumadhav, arXiv:1702.04724 (2017), arXiv:1702.04724 [gr-qc].

[41] G. P. Smith *et al.*, *IAU Symp.* **338**, 98 (2017), arXiv:1803.07851 [astro-ph.CO].

[42] K. Haris, A. K. Mehta, S. Kumar, T. Venumadhav, and P. Ajith, arXiv:1807.07062 (2018), arXiv:1807.07062 [gr-qc].

[43] M. Oguri, *Mon. Not. Roy. Astron. Soc.* **480**, 3842 (2018), arXiv:1807.02584 [astro-ph.CO].

[44] S.-S. Li, S. Mao, Y. Zhao, and Y. Lu, *Mon. Not. Roy. Astron. Soc.* **476**, 2220 (2018), arXiv:1802.05089 [astro-ph.CO].

[45] T. Broadhurst, J. M. Diego, and G. Smoot, arXiv:1802.05273 (2018), arXiv:1802.05273 [astro-ph.CO].

[46] T. Broadhurst, J. M. Diego, and G. F. Smoot, arXiv:1901.03190 (2019), arXiv:1901.03190 [astro-ph.CO].

[47] T. Broadhurst, J. M. Diego, and G. F. Smoot, arXiv:2006.13219 (2020), arXiv:2006.13219 [astro-ph.CO].

[48] J. M. Ezquiaga, D. E. Holz, W. Hu, M. Lagos, and R. M. Wald, *Phys. Rev. D* **103**, 064047 (2021), arXiv:2008.12814 [gr-qc].

[49] A. More and S. More, *Mon. Not. Roy. Astron. Soc.* **515**, 1044 (2022), arXiv:2111.03091 [astro-ph.CO].

[50] M. Çalışkan, J. M. Ezquiaga, O. A. Hannuksela, and D. E. Holz, *Phys. Rev. D* **107**, 063023 (2023), arXiv:2201.04619 [astro-ph.CO].

[51] A. Barsode, S. Goyal, and P. Ajith, *Astrophys. J.* **980**, 258 (2025), arXiv:2412.01278 [gr-qc].

[52] A. Vijaykumar, A. K. Mehta, and A. Ganguly, *Phys. Rev. D* **108**, 043036 (2023), arXiv:2202.06334 [gr-qc].

[53] S. Deguchi and W. D. Watson, *Astrophys. J.* **307**, 30 (1986).

[54] T. T. Nakamura, *Phys. Rev. Lett.* **80**, 1138 (1998).

[55] T. T. Nakamura and S. Deguchi, *Prog. Theor. Phys. Suppl.* **133**, 137 (1999).

[56] R. Takahashi and T. T. Nakamura, *Astrophys. J.* **595**, 1039 (2003), arXiv:astro-ph/0305055 [astro-ph].

[57] S. Jung and C. S. Shin, *Phys. Rev. Lett.* **122**, 041103 (2019), arXiv:1712.01396 [astro-ph.CO].

[58] X. Shan, C. Wei, and B. Hu, *Mon. Not. Roy. Astron. Soc.* **508**, 1253 (2021), arXiv:2012.08381 [astro-ph.CO].

[59] A. Mishra, A. K. Meena, A. More, S. Bose, and J. S. Bagla, *Mon. Not. Roy. Astron. Soc.* **508**, 4869 (2021), arXiv:2102.03946 [astro-ph.CO].

[60] A. K. Meena, A. Mishra, A. More, S. Bose, and J. S. Bagla, *Mon. Not. Roy. Astron. Soc.* **517**, 872 (2022), arXiv:2205.05409 [astro-ph.GA].

[61] R. Bondarescu, H. Ubach, O. Bulashenko, and A. P. Lundgren, *Phys. Rev. D* **108**, 084033 (2023), arXiv:2211.13604 [gr-qc].

[62] A. Mishra, A. K. Meena, A. More, and S. Bose, *Mon. Not. Roy. Astron. Soc.* **531**, 764 (2024), arXiv:2306.11479 [astro-ph.CO].

[63] A. Mishra, N. V. Krishnendu, and A. Ganguly, *Phys. Rev. D* **110**, 084009 (2024), arXiv:2311.08446 [gr-qc].

[64] P. Cremonese, J. M. Ezquiaga, and V. Salzano, *Phys. Rev. D* **104**, 023503 (2021), arXiv:2104.07055 [astro-ph.CO].

[65] P. Cremonese, D. F. Mota, and V. Salzano, *Annalen Phys.* **535**, 2300040 (2023), arXiv:2111.01163 [astro-ph.CO].

[66] X. Shan, X. Chen, B. Hu, and R.-G. Cai, arXiv:2301.06117 (2023), arXiv:2301.06117 [astro-ph.IM].

[67] N. Rao, A. Mishra, A. Ganguly, and A. More, arXiv:2510.17787 (2025), arXiv:2510.17787 [gr-qc].

[68] S. Basak, A. Ganguly, K. Haris, S. Kapadia, A. K. Mehta, and P. Ajith, *Astrophys. J.* **926**, L28 (2022), arXiv:2109.06456 [gr-qc].

[69] A. K. Lenon, A. H. Nitz, and D. A. Brown, *Mon. Not. Roy. Astron. Soc.* **497**, 1966 (2020), arXiv:2005.14146 [astro-ph.HE].

[70] I. M. Romero-Shaw, P. D. Lasky, and E. Thrane, *Astrophys. J.* **940**, 171 (2022), arXiv:2206.14695 [astro-ph.HE].

[71] H. L. Iglesias *et al.*, *Astrophys. J.* **972**, 65 (2024), arXiv:2208.01766 [gr-qc].

[72] R. Dhurkunde and A. H. Nitz, *Phys. Rev. D* **111**, 103018 (2025), arXiv:2311.00242 [astro-ph.HE].

[73] N. Gupte *et al.*, *Phys. Rev. D* **112**, 104045 (2025), arXiv:2404.14286 [gr-qc].

[74] K. Kacanja, K. Soni, and A. H. Nitz, arXiv:2508.00179 (2025), arXiv:2508.00179 [gr-qc].

[75] P. McMillin, K. J. Wagner, G. Ficarra, C. O. Lousto, and R. O'Shaughnessy, arXiv:2507.22862 (2025), arXiv:2507.22862 [gr-qc].

[76] A. G. Abac *et al.* (LIGO Scientific, Virgo, KAGRA), *Astrophys. J. Lett.* **993**, L21 (2025), arXiv:2510.26931 [astro-ph.HE].

[77] A. Tiwari, S. A. Bhat, M. A. Shaikh, and S. J. Kapaida, arXiv:2509.26152 (2025), arXiv:2509.26152 [astro-ph.HE].

[78] I. Romero-Shaw, J. Stegmann, H. Tagawa, D. Gerosa, J. Samsing, N. Gupte, and S. R. Green, *Phys. Rev. D* **112**, 063052 (2025), arXiv:2506.17105 [astro-ph.HE].

[79] P. C. Peters, *Phys. Rev.* **136**, B1224 (1964).

[80] H. A. Bethe and G. E. Brown, *Astrophys. J.* **506**, 780 (1998), arXiv:astro-ph/9802084.

[81] B. P. Abbott *et al.* (LIGO Scientific, Virgo), *Astrophys. J.* **883**, 149 (2019), arXiv:1907.09384 [astro-ph.HE].

[82] M. Mapelli, Formation Channels of Single and Binary Stellar-Mass Black Holes (2021) arXiv:2106.00699 [astro-ph.HE].

[83] M. Zevin, J. Samsing, C. Rodriguez, C.-J. Haster, and E. Ramirez-Ruiz, *Astrophys. J.* **871**, 91 (2019), arXiv:1810.00901 [astro-ph.HE].

[84] I. Cholis, E. D. Kovetz, Y. Ali-Haïmoud, S. Bird, M. Kamionkowski, J. B. Muñoz, and A. Raccanelli, *Phys. Rev. D* **94**, 084013 (2016), arXiv:1606.07437 [astro-ph.HE].

[85] L. Wen, *Astrophys. J.* **598**, 419 (2003), arXiv:astro-ph/0211492.

[86] F. Antonini, N. Murray, and S. Mikkola, *Astrophys. J.* **781**, 45 (2014), arXiv:1308.3674 [astro-ph.HE].

[87] K. K. Y. Ng, S. Vitale, W. M. Farr, and C. L. Rodriguez, *Astrophys. J. Lett.* **913**, L5 (2021), arXiv:2012.09876 [astro-ph.CO].

[88] H. Wang, I. Harry, A. Nitz, and Y.-M. Hu, *Phys. Rev. D* **109**, 063029 (2024), arXiv:2304.10340 [astro-ph.HE].

[89] T. Yang, R.-G. Cai, Z. Cao, and H. M. Lee, arXiv:2412.20664 (2024), arXiv:2412.20664 [gr-qc].

[90] I. Hinder, L. E. Kidder, and H. P. Pfeiffer, *Phys. Rev. D* **98**, 044015 (2018), arXiv:1709.02007 [gr-qc].

[91] L. Dai, S.-S. Li, B. Zackay, S. Mao, and Y. Lu, *Phys. Rev. D* **98**, 104029 (2018), arXiv:1810.00003 [gr-qc].

[92] K.-H. Lai, O. A. Hannuksela, A. Herrera-Martín, J. M. Diego, T. Broadhurst, and T. G. F. Li, *Phys. Rev. D* **98**, 083005 (2018), arXiv:1801.07840 [gr-qc].

[93] B. P. Abbott, R. Abbott, T. Abbott, S. Abraham, F. Acernese, K. Ackley, C. Adams, V. Adya, C. Affeldt, M. Agathos, *et al.*, Living reviews in relativity **23**, 1 (2020).

[94] G. Ashton *et al.*, *Astrophys. J. Suppl.* **241**, 27 (2019), arXiv:1811.02042 [astro-ph.IM].

[95] R. J. E. Smith, G. Ashton, A. Vajpeyi, and C. Talbot, *Mon. Not. Roy. Astron. Soc.* **498**, 4492 (2020), arXiv:1909.11873 [gr-qc].

[96] J. S. Speagle, *MNRAS* **493**, 3132 (2020), arXiv:1904.02180 [astro-ph.IM].

[97] H. Jeffreys, *The Theory of Probability*, Oxford Classic Texts in the Physical Sciences (1939).

[98] M. A. Shaikh, V. Varma, H. P. Pfeiffer, A. Ramos-Buades, and M. van de Meent, *Phys. Rev. D* **108**, 104007 (2023), arXiv:2302.11257 [gr-qc].

[99] M. A. Scheel *et al.*, *Class. Quant. Grav.* **42**, 195017 (2025), arXiv:2505.13378 [gr-qc].

[100] M. A. Shaikh, V. Varma, A. Ramos-Buades, H. P. Pfeiffer, M. Boyle, L. E. Kidder, and M. A. Scheel, *Class. Quant. Grav.* **42**, 195012 (2025), arXiv:2507.08345 [gr-qc].

[101] B. P. Abbott *et al.* (LIGO Scientific, Virgo), *Phys. Rev. Lett.* **116**, 061102 (2016), arXiv:1602.03837 [gr-qc].

[102] S. Khan, K. Chatzioannou, M. Hannam, and F. Ohme, *Phys. Rev. D* **100**, 024059 (2019), arXiv:1809.10113 [gr-qc].

[103] C. García-Quirós, M. Colleoni, S. Husa, H. Estellés, G. Pratten, A. Ramos-Buades, M. Mateu-Lucena, and R. Jaume, *Phys. Rev. D* **102**, 064002 (2020), arXiv:2001.10914 [gr-qc].

[104] G. Pratten *et al.*, *Phys. Rev. D* **103**, 104056 (2021), arXiv:2004.06503 [gr-qc].

[105] T. Damour and A. Nagar, *Phys. Rev. D* **90**, 044018 (2014), arXiv:1406.6913 [gr-qc].

[106] A. Nagar, T. Damour, C. Reisswig, and D. Pollney, *Phys. Rev. D* **93**, 044046 (2016), arXiv:1506.08457 [gr-qc].

[107] A. Nagar *et al.*, *Phys. Rev. D* **98**, 104052 (2018), arXiv:1806.01772 [gr-qc].

[108] A. Nagar, G. Pratten, G. Riemenschneider, and R. Gamba, *Phys. Rev. D* **101**, 024041 (2020), arXiv:1904.09550 [gr-qc].

[109] A. Nagar, G. Riemenschneider, G. Pratten, P. Rettigno, and F. Messina, *Phys. Rev. D* **102**, 024077 (2020), arXiv:2001.09082 [gr-qc].

[110] G. Riemenschneider, P. Rettigno, M. Breschi, A. Albertini, R. Gamba, S. Bernuzzi, and A. Nagar, *Phys. Rev. D* **104**, 104045 (2021), arXiv:2104.07533 [gr-qc].

[111] A. Nagar, P. Rettigno, R. Gamba, S. Albanesi, A. Albertini, and S. Bernuzzi, *Phys. Rev. D* **108**, 124018 (2023), arXiv:2304.09662 [gr-qc].

[112] E. O’Shea and P. Kumar, *Phys. Rev. D* **108**, 104018 (2023), arXiv:2107.07981 [astro-ph.HE].

[113] D. Chiaramello and A. Nagar, *Phys. Rev. D* **101**, 101501 (2020), arXiv:2001.11736 [gr-qc].

[114] M. Colleoni, F. A. R. Vidal, C. García-Quirós, S. Akçay, and S. Bera, *Phys. Rev. D* **111**, 104019 (2025), arXiv:2412.16721 [gr-qc].

[115] J. Calderón Bustillo, N. Sanchis-Gual, A. Torres-Forné, and J. A. Font, *Phys. Rev. Lett.* **126**, 201101 (2021), arXiv:2009.01066 [gr-qc].

[116] I. M. Romero-Shaw, P. D. Lasky, E. Thrane, and J. C. Bustillo, *Astrophys. J. Lett.* **903**, L5 (2020), arXiv:2009.04771 [astro-ph.HE].

[117] M. Favata, C. Kim, K. G. Arun, J. Kim, and H. W. Lee, *Phys. Rev. D* **105**, 023003 (2022), arXiv:2108.05861 [gr-qc].

[118] I. M. Romero-Shaw, D. Gerosa, and N. Loutrel, *Mon. Not. Roy. Astron. Soc.* **519**, 5352 (2023), arXiv:2211.07528 [astro-ph.HE].

[119] Y. Xu and E. Hamilton, *Phys. Rev. D* **107**, 103049 (2023), arXiv:2211.09561 [gr-qc].

[120] R. Hegde, N. Bose, and A. Pai, *Phys. Rev. D* **110**, 044026 (2024), arXiv:2310.13662 [gr-qc].

[121] B. G. Patterson, S. M. Tomson, and S. Fairhurst, *Phys. Rev. D* **111**, 044073 (2025), arXiv:2411.04187 [gr-qc].

[122] S. A. Bhat, A. Tiwari, M. A. Shaikh, and S. J. Kapadia, arXiv:2508.14850 (2025), arXiv:2508.14850 [gr-qc].

[123] S. Behnel, R. Bradshaw, C. Citro, L. Dalcin, D. S. Seljebotn, and K. Smith, *Computing in Science & Engineering* **13**, 31 (2011).

[124] C. R. Harris *et al.*, *Nature* **585**, 357 (2020), arXiv:2006.10256 [cs.MS].

[125] P. Virtanen *et al.*, *Nature Meth.* **17**, 261 (2020), arXiv:1907.10121 [cs.MS].

[126] A. Nitz *et al.*, *Pycbc* software, <https://github.com/gwastro/pycbc> (2024).

[127] LIGO Scientific Collaboration, LALSuite: LIGO Scientific Collaboration Algorithm Library Suite, Astrophysics Source Code Library, record ascl:2012.021 (2020), ascl:2012.021.

[128] C. Hoy and V. Raymond, *SoftwareX* **15**, 100765 (2021), arXiv:2006.06639 [astro-ph.IM].

[129] C. Talbot, R. Smith, E. Thrane, and G. B. Poole, *Phys. Rev. D* **100**, 043030 (2019), arXiv:1904.02863 [astro-ph.IM].

[130] J. D. Hunter, *Computing in Science & Engineering* **9**, 90 (2007).

[131] T. Kluyver *et al.*, in *Positioning and Power in Academic Publishing: Players, Agents and Agendas*, edited by F. Loizides and B. Schmidt (IOS Press, 2016) pp. 87 – 90.

[132] R. Abbott *et al.* (KAGRA, VIRGO, LIGO Scientific), *Phys. Rev. X* **13**, 011048 (2023), arXiv:2111.03634 [astro-ph.HE].

[133] C. Talbot, R. Smith, E. Thrane, and G. B. Poole, *Phys. Rev. D* **100**, 043030 (2019), arXiv:1904.02863 [astro-ph.IM].

[134] P. Madau and M. Dickinson, *Ann. Rev. Astron. Astrophys.* **52**, 415 (2014), arXiv:1403.0007 [astro-ph.CO].

[135] M. Fishbach, D. E. Holz, and W. M. Farr, *Astrophys. J. Lett.* **863**, L41 (2018), arXiv:1805.10270 [astro-ph.HE].

[136] P. A. R. Ade *et al.* (Planck), *Astron. Astrophys.* **594**, A13 (2016), arXiv:1502.01589 [astro-ph.CO].

[137] N. Cornish, L. Sampson, N. Yunes, and F. Pretorius, *Phys. Rev. D* **84**, 062003 (2011), arXiv:1105.2088 [gr-qc].

[138] P. Ajith, N. Fotopoulos, S. Privitera, A. Neunzert, and A. J. Weinstein, *Phys. Rev. D* **89**, 084041 (2014), arXiv:1210.6666 [gr-qc].

[139] J. A. Nelder and R. Mead, *Comput. J.* **7**, 308 (1965).